Ⓔ

Stochastic Generation of Accelerograms for Subduction Earthquakes

by Cristian Otarola and Sergio Ruiz

Abstract   The generation of accelerograms using stochastic methods has been a very useful methodology for solving the problem of the lack of appropriate strong-motion records for seismic design. Here, we propose the generation of synthetic strong motion for subduction earthquakes that present well-developed P waves and energetic arrivals of S waves associated with the main asperities of the source of these events. The first few seconds of these accelerograms are dominated by P waves; however, the strong motion is a mixture of S and P waves arriving at the same time. The traditional method considers only S waves. We propose to improve the stochastic generation of accelerograms taking into account a stratified velocity model, incident and azimuthal angles, free surface factors, and energy partition to incorporate the P and SV waves in the simulation. Finally, the simulated accelerograms are compared with the observed data recorded on rock by the Integrated Plate boundary Observatory Chile (IPOC) network during the 2007 Tocopilla and 2014 Iquique earthquakes. The use of P, SV, and SH waves in the stochastic simulation allowed us to generate three-component synthetic records. The early seconds are clearly associated with P waves, and the three components reproduce the shape and the amplitude in time and spectral domains for the observed and simulated records.

Online Material: Figures showing fit between observed and simulated waveforms, maximum amplitude of acceleration response spectra, peak ground velocities, and peak ground accelerations.

Introduction

Recently, two large earthquakes occurred in northern Chile: (1) the 2007 Tocopilla (M_w 7.8) and (2) the 2014 Iquique (M_w 8.1). These earthquakes were well recorded by strong-motion instruments of the Integrated Plate boundary Observatory Chile (IPOC) network, deployed in northern Chile to survey a well-identified seismic gap where no mega-earthquakes have occurred since 1877 (Kelleher, 1972; Comte and Pardo, 1991; Peyrat *et al.*, 2010; Ruiz *et al.*, 2014). The accelerograms recorded during both earthquakes show well-developed P waves and energetic arrivals of S waves associated with the main asperities of the source of these events (see Fig. 1). The first few seconds of the accelerograms are dominated by P waves; however, the strong motion is a mixture of S and P waves arriving at the same time.

The generation of accelerograms using stochastic methods (Boore, 1983, 2003) has been a very useful methodology for solving the problem of the lack of appropriate strong-motion records for seismic design. This idea was proposed by Hanks and McGuire (1981) who observed that the behavior of the accelerograms in the high-frequency range could be considered to be stochastic. Boore (1983), using some functional descriptions of the amplitude spectrum of ground motion (Aki, 1967; Brune, 1970), proposed to use a random phase spectrum, such that the simulated strong motion is distributed over a duration that depends on the earthquake magnitude and the hypocentral distance. The methodology of Boore (1983) has been improved by several authors: Beresnev and Atkinson (1997), Boore (2003), Motazedian and Atkinson (2005), among others. Accelerograms simulated using this method produced realistic results (Atkinson and Macias, 2009; Ugurhan *et al.*, 2012; Yalcinkaya *et al.*, 2012; Ghofrani *et al.*, 2013). Here, we propose to improve the stochastic generation of accelerograms, taking into account a stratified velocity model, incident and azimuthal angles, free surface factors, and energy partition, to incorporate the P and SV waves in the simulation. Finally, the simulated accelerograms are compared with the observed data recorded on rock by the IPOC network during the 2007 Tocopilla and 2014 Iquique earthquakes.

Methodology

Far-field displacement for P, SV, and SH waves is used to model the Fourier amplitude spectrum of acceleration in a
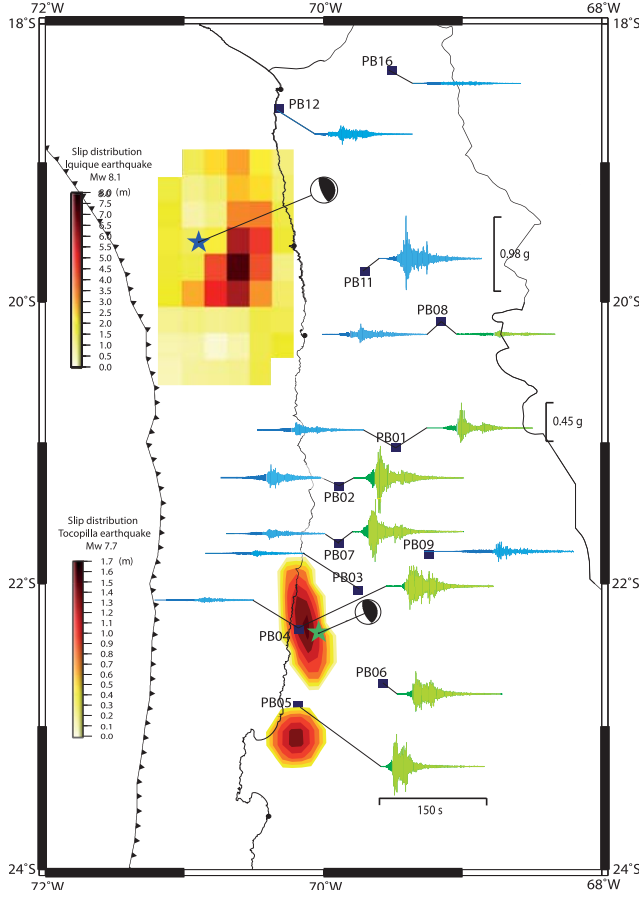
Figure 1. Slip distribution of the 2007 Tocopilla (Ruiz, 2012) and 2014 Iquique (Ruiz *et al.*, 2014) earthquakes. The blue squares are the Integrated Plate boundary Observatory Chile (IPOC) stations. The green star is the epicenter of the 2007 Tocopilla earthquake; the blue star is the epicenter of the 2014 Iquique earthquake; and the focal mechanisms are also shown. The darker color in the early seconds of the accelerograms correspond to the first seconds of *P* waves arrivals.

specific coordinate system. Following Aki and Richards (2002), equations (1)–(3) show the far-field displacement for the *P*, *SV*, and *SH* waves propagating in the ray direction:

$$\mathbf{u}^P(x,t) = \frac{\mathfrak{I}^P \dot{M}(t - r/\alpha)}{4\pi\rho\alpha^3 r}\hat{I} \tag{1}$$

$$\mathbf{u}^{SV}(x,t) = \frac{\mathfrak{I}^{SV} \dot{M}(t - r/\beta)}{4\pi\rho\beta^3 r}\hat{p} \tag{2}$$

$$\mathbf{u}^{SH}(x,t) = \frac{\mathfrak{I}^{SH} \dot{M}(t - r/\beta)}{4\pi\rho\beta^3 r}\hat{\varphi}, \tag{3}$$

in which $\hat{I}$, $\hat{p}$, and $\hat{\varphi}$ are unit vectors in the directions of *P*, *SV*, and *SH* motions, respectively. In addition, $\hat{I}$ and $\hat{p}$ are always in the incident or vertical plane, whereas $\hat{\varphi}$ is always orthogonal to this plane. $\mathfrak{I}^P$, $\mathfrak{I}^{SV}$, and $\mathfrak{I}^{SH}$ are the radiation patterns

for *P*, *SV*, and *SH* waves; $\dot{M}$ is the source time function; *r* is the hypocentral distance from the source to the observation point; ρ is the density in the vicinity of the source; and α and β are the *P*- and *S*-wave velocities.

We subdivided the fault plane of earthquakes into subfaults. Each subfault is considered as a point source (Beresnev and Atkinson, 1997). The acceleration waveforms due to a point source are obtained twice, differentiating equations (1)–(3) with respect to time. These ground motions are convoluted with the path and the site effects and rotated to radial, tangential, and vertical components. Finally, we modeled the Fourier spectrum of these synthetic records of *P*, *SV*, and *SH* waves following an $\omega^{-\gamma}$ model (Aki, 1967) for the source spectral shape, geometrical spreading and anelastic attenuation for the path, and the amplification and attenuation for the site, as was proposed by Boore (1983, 2003), which are given by the following:

$$A^P_{rij} = \frac{\langle R^P\rangle \mathrm{FS}^P_r \mathrm{PE}^P_r M_{0ij}}{4\pi\rho\alpha^3}\frac{(2\pi f)^2}{1 + (f/f_{Pcij})^{\gamma}}$$
$$G(R_{ij})\exp\left(\frac{-\pi f R_{ij}}{Q_P(f)\alpha}\right)\exp(-\pi f\kappa)\mathrm{Amp}(f) \tag{4}$$

$$A^P_{zij} = \frac{\langle R^P\rangle \mathrm{FS}^P_z \mathrm{PE}^P_z M_{0ij}}{4\pi\rho\alpha^3}\frac{(2\pi f)^2}{1 + (f/f_{Pcij})^{\gamma}}$$
$$G(R_{ij})\exp\left(\frac{-\pi f R_{ij}}{Q_P(f)\alpha}\right)\exp(-\pi f\kappa)\mathrm{Amp}(f) \tag{5}$$

$$A^{SV}_{rij} = \frac{\langle R^{SV}\rangle \mathrm{FS}^{SV}_r \mathrm{PE}^{SV}_r M_{0ij}}{4\pi\rho\beta^3}\frac{(2\pi f)^2}{1 + (f/f_{Scij})^{\gamma}}$$
$$G(R_{ij})\exp\left(\frac{-\pi f R_{ij}}{Q_S(f)\beta}\right)\exp(-\pi f\kappa)\mathrm{Amp}(f) \tag{6}$$

$$A^{SV}_{zij} = \frac{\langle R^{SV}\rangle \mathrm{FS}^{SV}_z \mathrm{PE}^{SV}_z M_{0ij}}{4\pi\rho\beta^3}\frac{(2\pi f)^2}{1 + (f/f_{Scij})^{\gamma}}$$
$$G(R_{ij})\exp\left(\frac{-\pi f R_{ij}}{Q_S(f)\beta}\right)\exp(-\pi f\kappa)\mathrm{Amp}(f) \tag{7}$$

$$A^{SH}_{hij} = \frac{\langle R^{SH}\rangle \mathrm{FS}^{SH}_h \mathrm{PE}^{SH}_h M_{0ij}}{4\pi\rho\beta^3}\frac{(2\pi f)^2}{1 + (f/f_{Scij})^{\gamma}}$$
$$G(R_{ij})\exp\left(\frac{-\pi f R_{ij}}{Q_S(f)\beta}\right)\exp(-\pi f\kappa)\mathrm{Amp}(f), \tag{8}$$

in which the superscripts *P*, *SV*, and *SH* denote *P*, *SV*, and *SH* waves, respectively. The subscripts *r*, *h*, and *z* correspond to radial, tangential, and vertical components. Each subfault of the finite-fault model is indicated by subscript *ij*, in which the subscripts *i* and *j* correspond to each subfault along the length and width (or vice versa) of the main fault. $\langle R^P\rangle$,

$\langle R^{SV} \rangle$, and $\langle R^{SH} \rangle$ are the analytical radiation coefficients of the P, SV, and SH waves, depending on the dip (δ) and rake (λ) angles of a source (Onishi and Horike, 2004). FS_r^P, FS_z^P, FS_r^{SV}, FS_z^{SV}, and FS_h^{SH} are the amplification factors due to the free surface (Evans, 1984; Jiang *et al.*, 1998). PE_r^P, PE_z^P, PE_r^{SV}, PE_z^{SV}, and PE_h^{SH} are the factors that model the partition of P, SV, and SH wave energy into r, h, and z components. α and β are the P- and S-wave velocities; M_{0ij} is the ijth sub-fault seismic moment; $G(R_{ij})$ is the geometrical spreading; $Q_S(f)$ and $Q_P(f)$ are the quality factors of the S and P waves; f_{Scij} is the dynamic frequency for the S waves in the subfault ij (Motazedian and Atkinson, 2005); and f_{Pcij} is the dynamic frequency for the P waves derived from the relation between the S-wave corner frequency (f_{Sc}) and the P-wave corner frequency like $f_{Pc} = (\alpha/\beta)f_{Sc}$ (Hanks and Wyss, 1972).

To obtain the FS and PE factors, we consider only the direct rays. The rays are propagated in a homogeneous horizontally layered velocity model. The Snell law is used to estimate the incident angle in each station. Finally, we obtain the FS and PE factors for P, SV, and SH. The FS factors are similar to those proposed by Jiang *et al.* (1998) and Evans (1984).

The PE factors considering the radial, tangential, and vertical components are

$$\hat{l} = \mathrm{PE}_r^P \hat{r} + \mathrm{PE}_z^P \hat{z} \tag{9}$$

$$\hat{p} = \mathrm{PE}_r^{SV} \hat{r} + \mathrm{PE}_z^{SV} \hat{z} \tag{10}$$

$$\hat{\varphi} = \mathrm{PE}_h^{SH} \hat{h}. \tag{11}$$

Then, if Θ is the incident angle for P or S seismic rays, PE factors are

$$\mathrm{PE}_r^P = -\sin(\Theta) \tag{12}$$

$$\mathrm{PE}_z^P = \cos(\Theta) \tag{13}$$

$$\mathrm{PE}_r^{SV} = \cos(\Theta) \tag{14}$$

$$\mathrm{PE}_z^{SV} = \sin(\Theta) \tag{15}$$

$$\mathrm{PE}_h^{SH} = 1. \tag{16}$$

The Fourier spectrum of acceleration for each subfault (equations 4–8) are transformed to time domain a_r^P, a_z^P, a_r^{SV}, a_z^{SV}, and a_h^{SH}. Then, we rotated the acceleration time series associated with each subfault considering the azimuth angle (φ_{ij}) to project them in the east–west, north–south, and vertical components. In this way, the acceleration time series of each subfault are multiplied by the scaling factors of the following:

$$H_{ij}^S = \frac{M_0}{M_{ij}} \sqrt{\frac{\sum_{f_k}[\frac{f_k^2}{1+(f_k/f_{Sc})^\gamma}]^2}{N\sum_{f_k}[\frac{f_k^2}{1+(f_k/f_{Scij})^\gamma}]^2}} \tag{17}$$

$$H_{ij}^P = \frac{M_0}{M_{ij}} \sqrt{\frac{\sum_{f_k}[\frac{f_k^2}{1+(f_k/f_{Pc})^\gamma}]^2}{N\sum_{f_k}[\frac{f_k^2}{1+(f_k/f_{Pcij})^\gamma}]^2}}, \tag{18}$$

in which M_0 is the total seismic moment, f_k is the kth frequency ordinate, H_{ij}^S and H_{ij}^P are the scaling factors for the S (Motazedian and Atkinson, 2005) and P waves for the ijth subfault that aims to conserve energy. In contrast to Motazedian and Atkinson (2005), we have considered that the total radiated energy is given by the sum of the radiated energy of the S and P waves.

The acceleration time series associated with each subfault are summed considering the phase associated with the time rupture (t_{rij}) of the ijth subfault and the travel time of the seismic waves (P and S) to the stations (t_{Vij}^P and t_{Vij}^S):

$$\Delta t_{ij}^P = t_{rij} + t_{Vij}^P \tag{19}$$

$$\Delta t_{ij}^S = t_{rij} + t_{Vij}^S, \tag{20}$$

in which Δt_{ij}^P and Δt_{ij}^S are the relative time delay for the P and S waves from the ijth subfault to the stations.

Finally, the accelerograms at the observation point in the east–west, north–south, and vertical components are obtained:

$$a_{\mathrm{EW}}(t) = \sum_{i=1}^{N_L} \sum_{j=1}^{N_W} [H_{ij}^S a_{\mathrm{EW}ij}^S(t + \Delta t_{ij}^S) + H_{ij}^P a_{\mathrm{EW}ij}^P(t + \Delta t_{ij}^P)] \tag{21}$$

$$a_{\mathrm{NS}}(t) = \sum_{i=1}^{N_L} \sum_{j=1}^{N_W} [H_{ij}^S a_{\mathrm{NS}ij}^S(t + \Delta t_{ij}^S) + H_{ij}^P a_{\mathrm{NS}ij}^P(t + \Delta t_{ij}^P)] \tag{22}$$

$$a_{\mathrm{Z}}(t) = \sum_{i=1}^{N_L} \sum_{j=1}^{N_W} [H_{ij}^S a_{\mathrm{Z}ij}^S(t + \Delta t_{ij}^S) + H_{ij}^P a_{\mathrm{Z}ij}^P(t + \Delta t_{ij}^P)], \tag{23}$$

in which N_L and N_W are the number of subfaults along length and width of main fault.

Figure 2 summarizes the proposed simulation method for the 2007 Tocopilla record at station PB08. In Figure 2a, white noise is generated for P, SV, and SH waves considering a duration given by the duration of the motion. In Figure 2b,
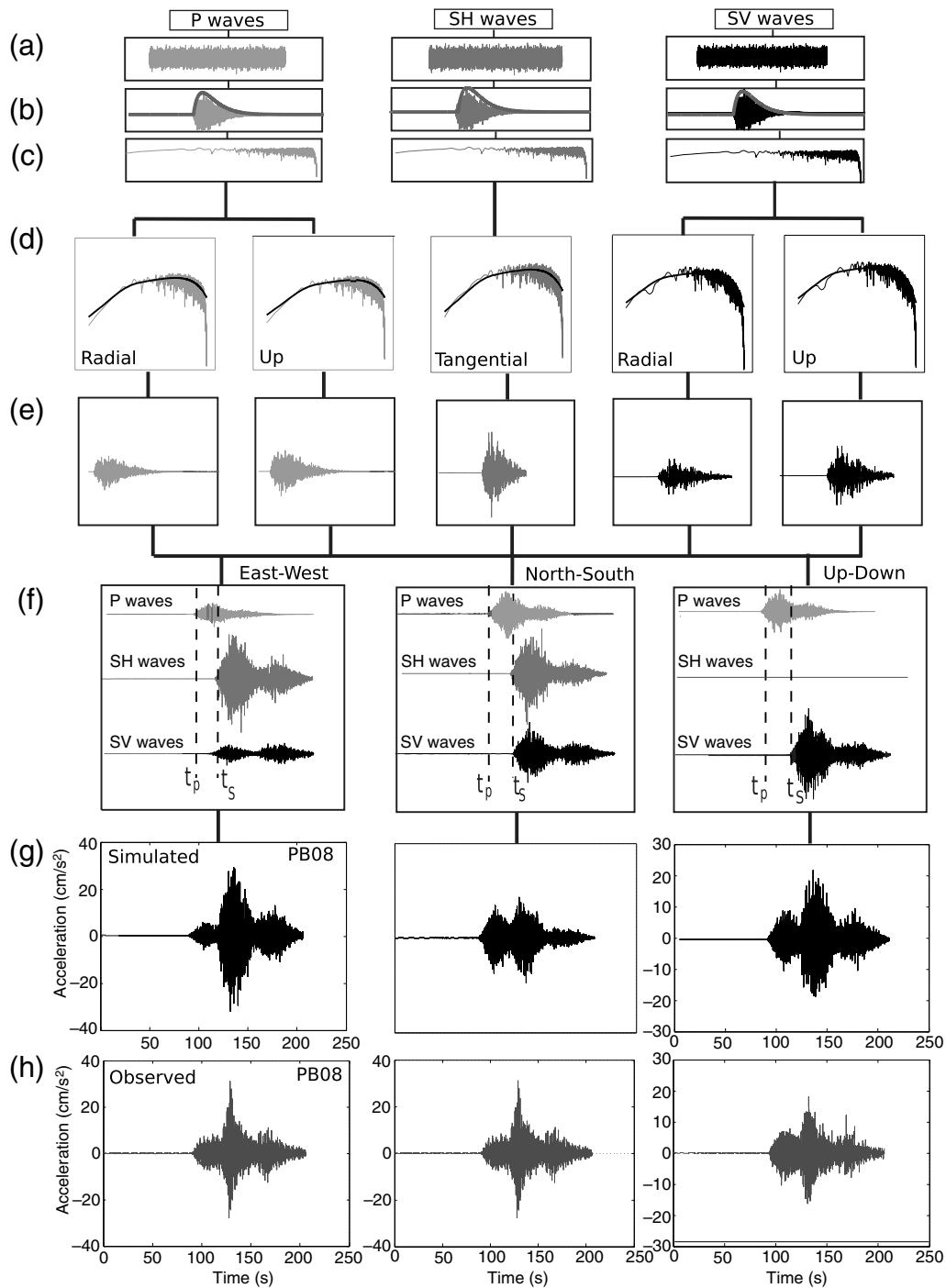
Figure 2. Schematic simulation of the PB08 strong-motion record for the 2007 Tocopilla earthquake. (a) White noise; (b) windowed noise; (c) normalized Fourier amplitude spectra of windowed noise; (d) shape-noise spectra modeled by the $\omega^{-\gamma}$ spectrum model. (e) The spectra are transformed to the time domain. (f) Rotation and addition of the time-series acceleration associated with each subfault into the east–west, north–south, and vertical components, for the *P*, *SV*, and *SH* waves. (g) Simulated records and (h) the observed data of the PB08 station for the 2007 Tocopilla earthquake.

a windowed white noise time series is modulated using a function of Saragoni and Hart (1974). Figure 2c shows the windowed noise transformed into the frequency domain (for each subfault) and normalized by the square root of the mean square amplitude spectrum. In Figure 2d, we multiplied the

spectral noise normalized by equations (4)–(8) to obtain the Fourier amplitude spectrum of acceleration of the *P*, *SV*, and *SH* waves for radial, tangential, and vertical components. In Figure 2e, we transform the spectra shown in Figure 2d to the time domain (accelerograms). In Figure 2f, we rotated the

Table 1
Input Parameters for the Accelerogram Simulation of the 2007 Tocopilla Earthquake

Factor	Parameter	Representative Value	Reference
Fine fault	L (km), W (km)	300, 200	Ruiz (2012)
	Strike (°), dip (°), rake (°)	26, 358, 109	Peyrat *et al.* (2010)
Source	Stress drop	34 bar	Seno (2014)
	Rupture velocity	2.65 km/s	Ruiz (2012)
	Density	3.3 g/cm^3	Peyrat *et al.* (2010)
	Velocity S waves	4.18 km/s	Husen *et al.* (1999)
	Velocity P waves	7.41 km/s	Husen *et al.* (1999)
	Hypocenter depth	47 km	Peyrat *et al.* (2010)
	Pulsing in percentage	8.83%	Ruiz (2012)
Path	Quality factor P waves	$Q_P(f) = 1350 f^{0.4}$	This study (trial and error)
	Quality factor S waves	$Q_S(f) = 600 f^{0.4}$	This study (trial and error)
	Geometric spreading	$1/R$, $R \leq 50$	This study (trial and error)
		$(\frac{1}{50})(\frac{50}{R})^{-0.1}$, $50 < R \leq 100$	
		$(\frac{1}{50})(\frac{50}{100})^{-0.1}(\frac{100}{R})^{1.4}$, $100 < R$	
	Average of the radiation pattern of the P waves	$\langle R^P \rangle = 0.5164$	Onishi and Horike (2004) This
	Average of the radiation pattern of the SV waves	$\langle R^{SV} \rangle = 0.3891$	study considering $\theta = 26°$ (dip)
	Average of the radiation pattern of the SH waves	$\langle R^{SH} \rangle = 0.3806$	and $\varphi = 109°$ (rake)
Site	Kappa effects	$\kappa = 0.03$ s	Lancieri *et al.* (2012)
	Amplification	Amp$(f) = 1$	Station on hard rock
Velocity model	Stratified velocity model		Husen *et al.* (1999)

If R, seismic moment, and frequency units are km, dyn·cm, and 1/s, respectively, equations (4)–(8) should be multiplied by a factor 10^{-20} to express the strong ground motion in cgs units.

acceleration time series associated with each subfault, with respect to the azimuth angle. The accelerograms are projected in the east–west, north–south, and vertical components. Finally, the acceleration time series computed for each subfault are summed. Figure 2g shows the final simulated accelerograms for the three components of the record at station PB08, and Figure 2h shows the observed data. The proposed methodology reproduces adequately the amplitude and shape of the accelerogram at station PB08 for the three components (Fig. 2g,h). Then, we show the results for the records obtained on rock during the 2007 Tocopilla and 2014 Iquique Chilean subduction earthquakes.

Simulated Accelerograms of the 2007 Tocopilla and 2014 Iquique Earthquakes

Figure 1 shows the slip distribution of the Tocopilla M_w 7.8 and Iquique M_w 8.1 interplate thrust earthquakes. Both earthquakes were well recorded by accelerographs installed on rock. These records are simulated and compared with the observed data to test our proposed stochastic methodology. The northern Chile earthquakes occurred inside the seismic gap where the last mega-earthquake happened in 1877 ($M_w > 8.5$; Kelleher, 1972; Comte and Pardo, 1991). The 2007 Tocopilla earthquake (Peyrat *et al.*, 2010) occurred in the southern part of the seismic gap, in the deeper part of the seismogenic contact. The M_w 8.1 Iquique earthquake took place in the middle of the seismic gap, in the upper zone of the seismogenic contact (Hayes *et al.*, 2014; Lay *et al.*, 2014; Ruiz *et al.*, 2014; Schurr *et al.*, 2014). The rupture process and finite-fault model used for the Tocopilla earthquake are similar to that proposed by Peyrat *et al.* (2010) and modified by Ruiz

(2012). For the 2014 Iquique earthquake, we use the finite-fault model proposed by Ruiz *et al.* (2014) (Fig. 1).

The parameters used in the simulation are shown in Tables 1 and 2 for the 2007 Tocopilla and 2014 Iquique earthquakes. The quality factors and geometrical spreading are proposed for these earthquakes after several trial-and-error assays, due to the lack of information about these parameters for this study zone. The observed and simulated accelerograms of the 2007 Tocopilla and 2014 Iquique earthquakes are shown in Figures 3–6 and Ⓔ Figures S1–S4 (available in the electronic supplement to this article). The figures show the simulated and observed accelerograms and the acceleration response spectra for 5% damping. The observed and synthetic accelerograms have been filtered between 0.1 and 20 Hz using a Butterworth fourth-order filter; the response instrumental, mean, and trend was removed for the real data. We compare the observed and simulated records using the model bias and standard error. The residual between the observed and simulated acceleration response spectral of 5% damping at period T_i for the jth station is given by Graves and Pitarka (2010):

$$r_j(T_i) = \ln\left[\frac{O_j(T_i)}{S_j(T_i)}\right], \qquad (24)$$

in which $O_j(T_i)$ and $S_j(T_i)$ are the observed and simulated spectral of acceleration, respectively.

The model bias is then given by

$$B(T_i) = \frac{1}{N}\sum_{j=1}^{N} r_j(T_i), \qquad (25)$$

and the standard error by

Table 2
Input Parameters for the Accelerogram Simulation of the 2014 Iquique Earthquake

Factor	Parameter	Representative Value	Reference
Fine fault	L (km), W (km)	150, 95	Ruiz *et al.* (2014)
	Strike (°), dip (°), rake (°)	18, 358, 109	Ruiz *et al.* (2014)
Source	Stress drop	25 bar	Seno (2014)
	Rupture velocity	1.5 km/s	Ruiz *et al.* (2014)
	Density	3.0 g/cm³	Peyrat *et al.* (2010)
	Velocity S waves	3.87 km/s	Husen *et al.* (1999)
	Velocity P waves	6.95 km/s	Husen *et al.* (1999)
	Hypocenter depth	20 km	Ruiz *et al.* (2014)
	Pulsing in percentage	100%	Ruiz *et al.* (2014)
Path	Quality factor P waves	$Q_P(f) = 1350 f^{0.4}$	This study (trial and error)
	Quality factor S waves	$Q_S(f) = 600 f^{0.4}$	This study (trial and error)
	Geometric spreading	$1/R$, $R \le 50$	This study (trial and error)
		$(\frac{1}{50})(\frac{50}{R})^{-0.1}$, $50 < R \le 100$	
		$(\frac{1}{50})(\frac{50}{100})^{-0.1}(\frac{100}{R})^{1.4}$, $100 < R$	
	Average of the radiation patron of the P waves	$\langle R^P \rangle = 0.5164$	Onishi and Horike (2004) This
	Average of the radiation patron of the SV waves	$\langle R^{SV} \rangle = 0.3911$	study considering $\theta = 18°$
	Average of the Radiation patron of the SH waves	$\langle R^{SH} \rangle = 0.3785$	and $\varphi = 109°$
Site	Kappa effects	$\kappa = 0.03$ s	Lancieri *et al.* (2012)
	Amplification	Amp(f) = 1	Station on hard rock
Velocity model	Stratified velocity model		Husen *et al.* (1999)

If R, seismic moment, and frequency units are km, dyn·cm, and 1/s, respectively, equations (4)–(8) should be multiplied by a factor 10^{-20} to express the strong ground motion in cgs units.

$$\sigma(T_i) = \left(\frac{1}{N} \sum_{j=1}^{N} [r_j(T_i) - B(T_i)]^2 \right)^{1/2}, \qquad (26)$$

in which N is the total number of stations.

Figure 7 shows the model bias (equation 25) and the standard error (equation 26) for the 2007 Tocopilla and 2014 Iquique earthquakes. For these comparisons, we only consider stations with epicentral distances less than 300 km. In this figure, we do not consider the stations PB09 and PB11 because the observed data show higher amplitudes than the simulated records, maybe due to site effects. This figure shows the goodness of fits (GOFs) for the three components of ground motion used for the Tocopilla and Iquique earthquakes. The heavy black line shows the bias, the shaded region shows the standard error, and the thin line shows the zero bias $(B(T_i) = 0)$, which indicates that simulation matches the observed acceleration response spectra of 5% damping. This figure exhibits, for both simulations, a little systematic model bias across a wide period range. The standard error ranges from ∼0.3 to 0.7 natural log units for the Tocopilla earthquake and from ∼0.4 to 0.6 natural log units for the Iquique earthquakes.

Additionally, our results are compared with the simulations of Tocopilla and Iquique records using the traditional stochastic method (Boore, 2003; Motazedian and Atkinson, 2005); for the S waves radiation pattern, we use the root mean square averages over the focal sphere (Boore and Boatwright, 1984), and the other parameters are the same shown in Tables 1 and 2 (see Ⓔ Figs. S8 and S9). Ⓔ Figure S10 shows the GOF for the average horizontal (geometric mean) components of ground motion for the Tocopilla and Iquique earthquakes. This figure exhibits an accentuated overpredic-

tion of the observations across a wide period range. The standard error ranges from ∼0.2 to 0.6 natural log units for the Tocopilla earthquake and from ∼0.2 to 0.7 natural log units for the Iquique earthquake. Ⓔ Figure S11 summarizes the spectral acceleration modeling bias (from equation 25) for the east–west and north–south components using the proposed methodology and average horizontal components (geometric mean) for the traditional method.

Discussion and Conclusions

The use of P, SV, and SH waves in the stochastic simulation allowed us to generate three-component synthetic records. The early seconds are clearly associated with P waves, and the three components reproduce the shape and the amplitude in time and spectral domains for the observed and simulated records. Figures 3–6 and Ⓔ Figures S1–S4, S6, and S7 show the comparison between observed and simulated accelerograms for the 2007 Tocopilla and 2014 Iquique earthquakes. These figures show a good agreement in amplitude and shape. In general, we observe that for the Tocopilla earthquake the simulated records reproduce adequately the important seismic arrivals associated with the two main asperities of the fault (Ruiz *et al.*, 2011). However, the shape and amplitude of the accelerograms of the Iquique earthquake are not as well reproduced. We think that the shape of the simulated data is strongly dependent on the finite-fault model used, so that we expect if we use a more detailed finite-fault model for the 2014 Iquique earthquake, these results can be improved. Another cause of this discrepancy could be associated with the use of only direct rays; this simplification implies that the FS and PE factors are not well
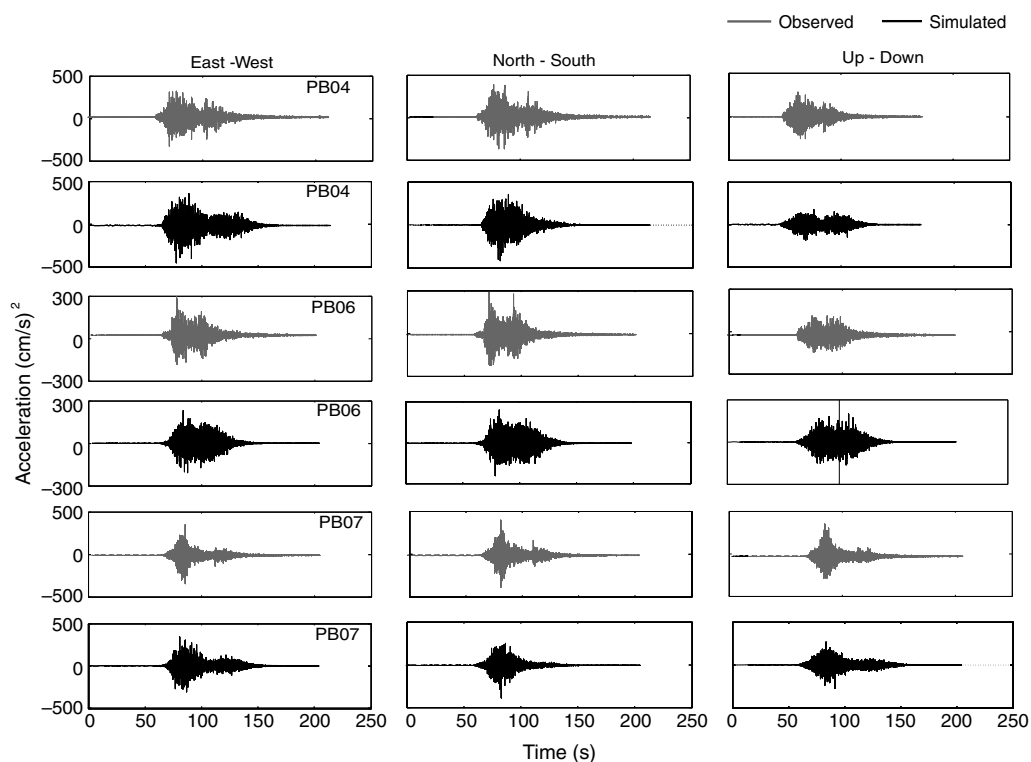
Figure 3. Simulated and observed accelerograms at stations PB04, PB06, and PB07 for the 2007 Tocopilla earthquake. The comparison with the other accelerograms recorded by the IPOC networks is shown in ⓔ Figure S1 (available in the electronic supplement to this article).
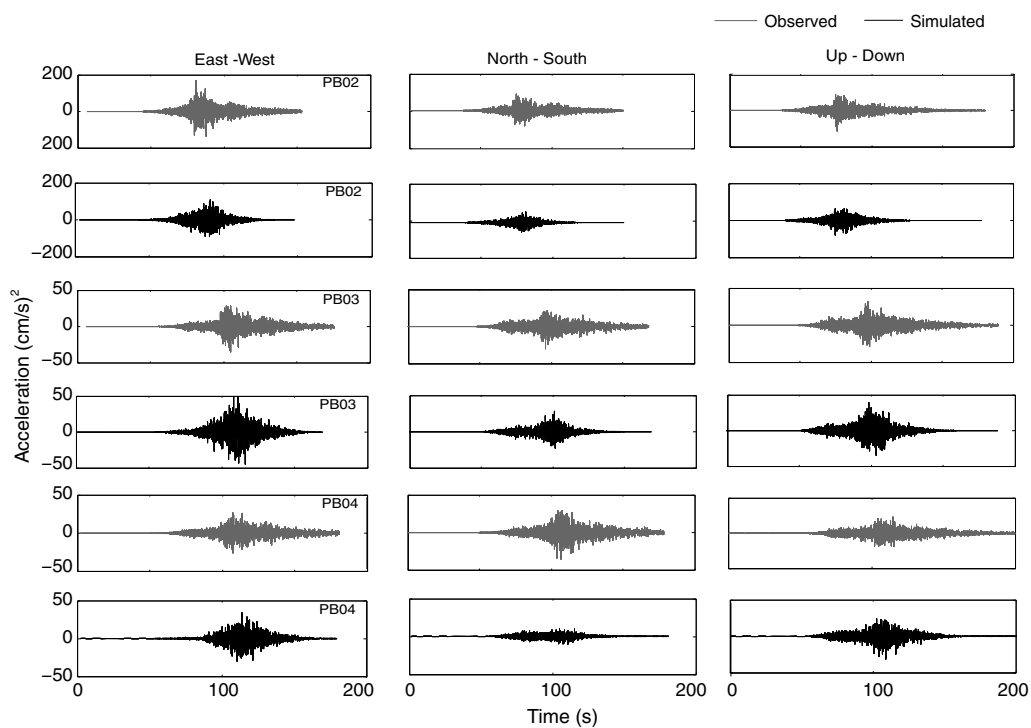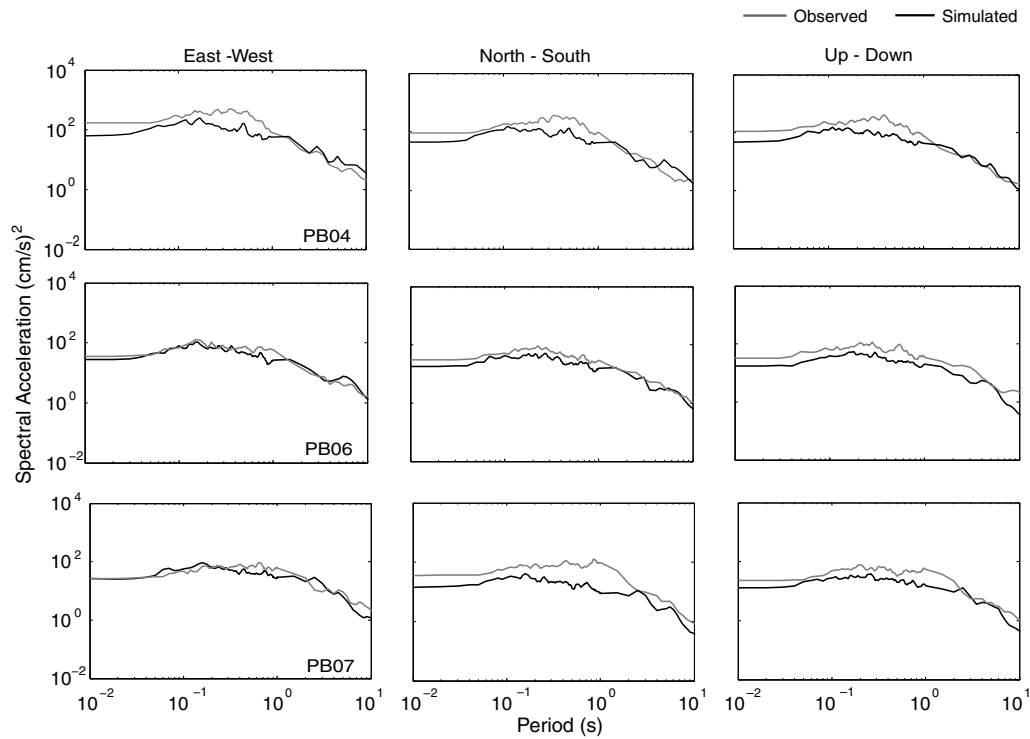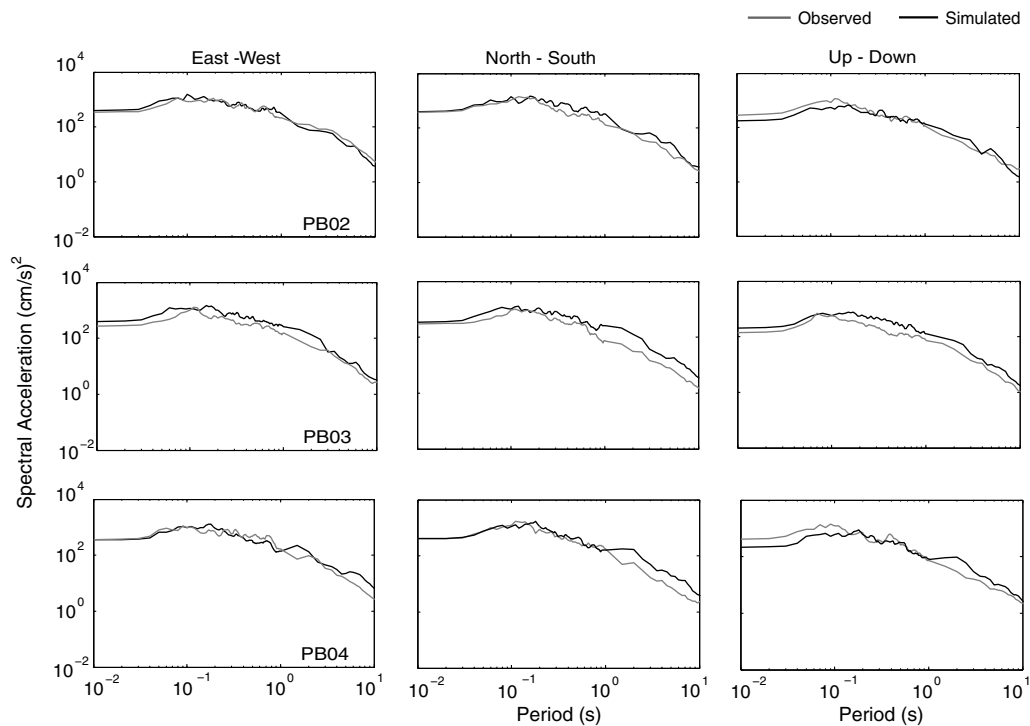

Figure 4. Simulated and observed accelerograms for stations PB02, PB03, and PB04 for the 2004 Iquique earthquake. The comparison with the other accelerograms recorded by the IPOC networks is shown in ⓔ Figure S2.

BSSA Early Edition

Figure 5. Simulated and observed acceleration response spectra for 5% damping at stations PB04, PB06, and PB07 for the 2007 To-copilla earthquake. The comparison with the other accelerograms recorded by the IPOC networks is shown in Ⓔ Figure S3.

Figure 6. Simulated and observed acceleration response spectra for 5% damping at stations PB04, PB06, and PB07 for the 2004 Iquique earthquake. The comparison with the other accelerograms recorded by the IPOC networks is shown in Ⓔ Figure S3.

solved by potential reflected or refracted rays. Actually, the position of the slip distribution of the 2014 Iquique earthquake, located near the trench, seems to favor the presence

of reflected and refracted waves, in contrast with the 2007 Tocopilla earthquake, where the slip distribution is located in the deeper zone of the seismogenic contact (Fig. 1). For the
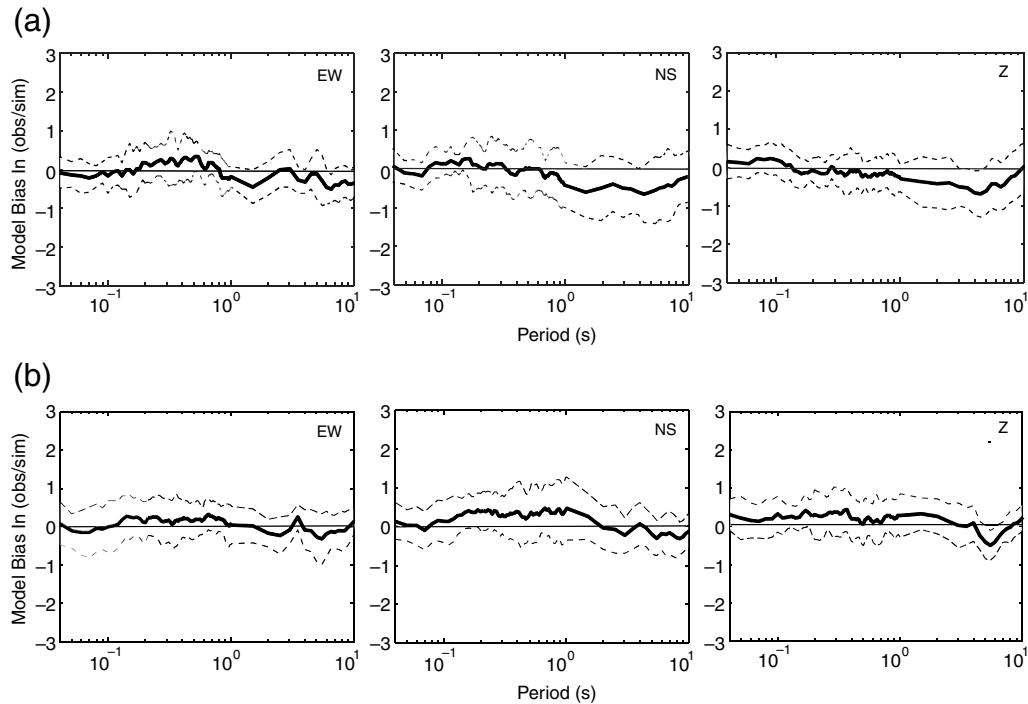
Figure 7. The goodness of fits (GOFs) between observed and simulated acceleration response spectra of 5% damping for (a) the 2007 Tocopilla earthquake and (b) the 2014 Iquique earthquake. The heavy line shows the bias, and the shaded region shows the standard error.

Iquique earthquake, there were two records that we could not reproduce properly: PB09 and PB11 (see Ⓔ Figs. S2, S4, and S5). We think that these stations may be affected by site effects, because the simulated records have systematically less amplitude for all periods.

Figure 7 shows a little systematic model bias and a standard error ranges between 0.3 and 0.7 natural log units in the comparison between observed and simulated records. Then, the simulated records reproduce the main characteristics of the ground-motion response spectra. The Tocopilla earthquake simulation shows a slight overprediction (negative bias) at periods above 1 s. This could be a consequence of the slip distribution that does not reproduce the complexities of the seismic rupture. On the other hand, the simulation considering *P*, *SV*, and *SH* waves improves the simulated records considering shape, duration, and amplitude, especially for the farthest stations to the source, which is more noticeable for the simulations of accelerograms for the 2014 Iquique earthquake (Ⓔ Fig. S9). Ⓔ Figure S11 resumes the model bias for both methodologies; the traditional method shows a systematic overprediction of the ground-motion simulations for the 2007 Tocopilla earthquake and especially for the 2014 Iquique earthquake (Ⓔ Fig. S10), in contrast with our proposed simulation where the bias is lower.

Finally, we consider that the proposed methodology, which incorporates physical characteristics of the seismic rupture of earthquakes, improves the simulation of strong-motion records of subduction earthquakes. The most significant parameters incorporated in our methodology are the incident angle of the seismic rays, PS and PE factors, and the radiation coefficients of the *P*, *SV*, and *SH* waves. We expect, in the future, to consider the arrival of reflected and refracted rays. For the moment, the reflected and refracted waves are incorporated indirectly in the geometrical spreading (Tables 1 and 2). Here, we use the analytical expressions proposed by Onishi and Horike (2004), but more precise simulations could be obtained calculating numerically the radiation coefficients of the *P*, *SV*, and *SH* waves averaged over azimuths and a range of takeoff angles for specific strike, dip, and rake, as proposed by Boore and Boatwright (1984).

Data and Resources

The strong-motion data used in this study were collected from the Integrated Plate boundary Observatory Chile (IPOC), doi: 10.14470/PK615318.

Acknowledgments

References

Aki, K. (1967). Scaling law of seismic spectrum, *J. Geophys. Res.* **72,** 1217–1231.

Aki, K., and P. Richards (2002). *Quantitative Seismology*, Second Ed., University Science Books, Sausalito, California.

Atkinson, G. M., and M. Macias (2009). Predicted ground motions for great interface earthquakes in the Cascadia subduction zone, *Bull. Seismol. Soc. Am.* **99,** 1552–1578.

Beresnev, I. A., and G. M. Atkinson (1997). Modelling finite fault radiation from ω^n spectrum, *Bull. Seismol. Soc. Am.* **87,** 67–84.

Boore, D. M. (1983). Stochastic simulation of high-frequency ground motions based on seismological models of the radiated spectra, *Bull. Seismol. Soc. Am.* **73,** 1865–1894.

Boore, D. M. (2003). Simulation of ground motion using the stochastic method, *Pure Appl. Geophys.* **160,** 635–675.

Boore, D. M., and J. Boatwright (1984). Average body-wave radiation coefficients, *Bull. Seismol. Soc. Am.* **74,** 1615–1621.

Brune, J. N. (1970). Tectonic stress and the spectra of seismic shear waves from earthquakes, *J. Geophys. Res.* **75,** 4997–5009.

Comte, D., and M. Pardo (1991). Reappraisal of great historic earthquakes in the northern Chile and southern Peru seismic gaps, *Nat. Hazards* **4,** 23–44.

Evans, R. (1984). Effects of the free surface on shear wavetrains, *Geophys. J. Roy. Astron. Soc.* **76,** 165–172.

Ghofrani, H., G. Atkinson, K. Goda, and K. Assatourians (2013). Stochastic finite-fault simulations of the 11th March Tohoku, Japan earthquake, *Bull. Seismol. Soc. Am.* **103,** 1307–1320.

Graves, R. W., and A. Pitarka (2010). Broadband ground-motion simulation using a hybrid approach, *Bull. Seismol. Soc. Am.* **100,** 2095–2123.

Hanks, T. C., and R. K. McGuire (1981). The character of high-frequency strong ground motion, *Bull. Seismol. Soc. Am.* **71,** 2071–2095.

Hanks, T. C., and M. Wyss (1972). The use of body-wave spectra in the determination of seismic-source parameters, *Bull. Seismol. Soc. Am.* **62,** 561–589.

Hayes, G. P., M. W. Herman, W. D. Barnhart, K. P. Furlong, S. Riquelme, H. M. Benz, E. Bergman, S. Barrientos, P. S. Earle, and S. Samsonov (2014). Continuing megathrust earthquake potential in Chile after the 2014 Iquique earthquake, *Nature* **512,** 295–298.

Husen, S., E. Kissling, E. Flueh, and G. Asch (1999). Accurate hypocentre determination in the seismogenic zone of the subducting Nazca plate in northern Chile using a combined on-offshore network, *Geophys. J. Int.* **138,** 687–701.

Jiang, J., G. Baird, and D. Blair (1998). Polarization and amplitude attributes of reflected plane and spherical waves, *Geophys. J. Int.* **132,** 577–583.

Kelleher, J. A. (1972). Rupture zones of large South American earthquakes and some predictions, *J. Geophys. Res.* **77,** 2087–2103.

Lancieri, M., R. Madariaga, and F. Bonilla (2012). Spectral scaling of the aftershocks of the Tocopilla 2007 earthquake in northern Chile, *Geophys. J. Int.* **188,** 469–480.

Lay, Th., H. Yue, E. Brodsky, and C. An (2014). The 1 April 2014 Iquique, Chile, M_w 8.1 earthquake rupture sequence, *Geophys. Res. Lett.* **41,** 3818–3825.

Motazedian, D., and G. M. Atkinson (2005). Stochastic finite-fault modeling based on a dynamic corner frequency, *Bull. Seismol. Soc. Am.* **95,** 995–1010.

Onishi, Y., and M. Horike (2004). The extended stochastic simulation method for close-fault earthquake motion prediction and comments for its application to the hybrid method, *J. Struct. Constr. Eng., AIJ* **586,** 37–44.

Peyrat, S., R. Madariaga, E. Buforn, J. Campos, G. Asch, and J. P. Vilotte (2010). Kinematic rupture process of the 2007 Tocopilla earthquake and its main aftershocks from teleseismic and strong-motion data, *Geophys. J. Int.* **182,** 1411–1430.

Ruiz, S. (2012). Kinematic and dynamic inversions of subduction earthquakes using strong motion and cGPS data, *Ph.D. Thesis*, University of Chile, Chile and Institut de Physique du Globe de Paris, France.

Ruiz, S., E. Kausel, J. Campos, G. R. Saragoni, and R. Madariaga (2011). Identification of high frequency pulses from earthquake asperities along Chilean subduction zone using strong motion, *Pure Appl. Geophys.* **168,** 125–139.

Ruiz, S., M. Metois, A. Fuenzalida, J. Ruiz, F. Leyton, R. Grandin, C. Vigny, R. Madariaga, and J. Campos (2014). Intense foreshocks and a slow slip event preceded the 2014 Iquique M_w 8.1 earthquake, *Science* **345,** no. 6201, 1165–1169, doi: 10.1126/science.1256074.

Saragoni, G. R., and G. C. Hart (1974). Simulation of artificial earthquakes, *Earthq. Eng. Struct. Dynam.* **2,** 249–267.

Schurr, B., G. Asch, S. Hainzl, J. Bedford, A. Hoechner, M. Palo, R. Wang, M. Moreno, M. Bartsch, and Y. Zhang (2014). Gradual unlocking of plate boundary controlled initiation of the 2014 Iquique earthquake, *Nature* **512,** 299–302, doi: 10.1038/nature13681.

Seno, T. (2014). Stress drop as a criterion to differentiate subduction zones where M_w 9 earthquakes can occur, *Tectonophysics* **621,** 198–210.

Ugurhan, B., A. Askan, A. Akinci, and L. Malagnini (2012). Strong ground motion simulation of the 6 April 2009 L'Aquila, Italy, earthquake, *Bull. Seismol. Soc. Am.* **102,** 429–1445.

Yalcinkaya, E., A. Pinar, O. Uskuloglu, S. Tekebas, and B. Firat (2012). Selecting the most suitable rupture model for the stochastic simulation of the 1999 Izmit earthquake and prediction of peak ground motions, *Soil Dynam. Earthq. Eng.* **42,** 1–16.

Facultad de Ciencias Físicas y Matemáticas
Universidad de Chile
Blanco Encalada 2002
Santiago, Chile 8370449
crotarola@ug.uchile.cl
sruiz@dgf.uchile.cl